AIAA JOURNAL
Vol. 46, No. 4, April 2008

Deriving Lifetime Maps of Coherent Structures in the Turbulent Boundary Layer

Dan Palumbo*
NASA Langley Research Center, Hampton, Virginia, 23681

DOI: 10.2514/1.30644

The lifetimes of coherent structures are derived from data correlated over a three-sensor array sampling streamwise sidewall pressure at high Reynolds number ($>10^8$). The data were acquired at subsonic, transonic, and supersonic speeds aboard a Tupolev Tu-144. The lifetimes are computed from a variant of the correlation length termed the *lifelength*. *Characteristic lifelengths* are estimated by fitting a Gaussian distribution to the sensors' cross spectra and are shown to compare favorably with Efimtsov's prediction of correlation space scales. Lifelength distributions are computed in the time/frequency domain using an interval correlation technique on the continuous wavelet transform of the original time data. The median values of the lifelength distributions are found to be very close to the frequency-averaged result. The interval correlation technique is shown to allow the retrieval and inspection of the original time data of each event in the lifelength distributions, thus providing a means to locate and study the nature of the coherent structure in the turbulent boundary layer. The lifelength data are converted to lifetimes using the convection velocity. The lifetime of events in the time/frequency domain are displayed in lifetime maps. The primary purpose of the paper is to validate these new analysis techniques so that they can be used with confidence to further characterize the behavior of coherent structures in the turbulent boundary layer.

Nomenclature

a	=	wavelet scale factor
c	=	speed of sound in air
C_f	=	coefficient of skin friction
$C(a,t)$	=	continuous, scaled, wavelet transform
Δt	=	time delay between sensors
F_a	=	scaled frequency
f_b	=	Gaussian shape factor
f_c	=	wavelet center frequency
H	=	Hermitian operator
$\mathrm{ic}_{r,2,i}$	=	interval correlation between reference sensor r, and sensor i, scaled by sensor 2
M	=	Mach number
PC_1	=	first principal component of sensor array
Re	=	Reynolds number
$\mathbf{S}$	=	singular values matrix
$s(t)$	=	time data
Sr	=	Strouhal number
TD	=	matrix of time-delayed data
$\mathbf{td_i}$	=	delayed time data from sensor i
$\mathbf{td_r}$	=	delayed time data from reference sensor
$\mathbf{U}$	=	left singular matrix
U_∞	=	freestream velocity
U_c	=	convection velocity
U_τ	=	friction velocity
$\mathbf{V}$	=	right singular matrix
$W(t)$	=	wavelet filtered data
Δ	=	acquisition sample time
δ	=	boundary-layer thickness
Λ	=	correlation space scale
$\hat{\Lambda}$	=	estimated correlation space scale
ν	=	kinematic viscosity
φ	=	cross spectrum
Ψ_{Mor}	=	Morlet wavelet shape function
ω	=	angular frequency

Presented as Paper 2410 at the 12th AIAA/CEAS Aeroacoustics Conference (27th AIAA Aeroacoustics Conference), Cambridge, MA, 8–10 May 2006; received 23 February 2007; revision received 27 September 2007; accepted for publication 29 September 2007.

*Senior Aerospace Technologist, Structural Acoustics Branch, Mail Stop 463. Member AIAA.

I. Introduction

THE presence of coherence structure in the turbulent boundary layer (TBL) has been studied for decades, see Robinson [1] and Gad-el-Hak [2] for overviews of the topic. The payoff returned as a result of achieving an understanding of the behavior of coherent structures is that the dynamics of the turbulent boundary layer would be better understood leading to means of further reducing drag. Although much progress has been made at low Reynolds numbers, few results have been obtained at high Reynolds numbers due to difficulties in acquiring data in this regime either experimentally or through simulation. The technique introduced here uses an extension of an interval correlation approach [3] to estimate the size and lifetime of the coherent structures. Interval correlation is similar to other conditional sampling methods such as the variable-interval time average method (VITA) [4] and the $u'v'$ quadrant method [5]. Interval correlation differs from these methods in the property sensed, pressure as opposed to velocity, and the assumptions made about the nature of the structure. Interval correlation assumes only that the phase is constant over the sensor array and that the correlation distribution is Gaussian. This paper is concerned primarily with validating the approach as some of the results may be considered atypical and confidence in the technique must be gained before conclusions are drawn. Most established procedures to which this technique can be compared [6,7] are based on frequency-averaged data. The key benefit of the interval correlation technique is that the coherent structure can be located and its instantaneous behavior studied in the time domain.

Although the final result of this paper is the display of coherent structure lifetimes in the time/frequency domain, the data are acquired in the space/time domain with the lifetimes derived from measurements of correlated behavior in the spatial dimension. The term most commonly used to describe correlation in space is *correlation length* which, as defined by Corcos [6], assumes an exponential decay. This works well when deriving frequency-averaged statistics referenced to a single, upstream sensor. It is desired here to capture individual events relating to the passage of a coherent structure over the sensor array, so that the correlation envelope must be an even function centered over the array. A

function which meets this requirement and is strongly related to the exponential is the Gaussian distribution. It will be shown later that the Gaussian distribution produces results very close to the exponential. To define the Gaussian distribution, a new term, characteristic lifelength, is introduced. The characteristic lifelength is the value of a parameter which fits the Gaussian distribution to data correlated over the sensor array. If the analysis were performed in time, rather than space, it would be called a lifetime. The event lifetime can be computed from the lifelength using the convection velocity. The characteristic lifelength is shown to be related to Efimtsov's correlation space scales [7] with results comparing favorably with Efimtsov's frequency-averaged predictions. The Gaussian distribution is preferred to the pure exponential because the analysis is performed on an interval bounding zero where the exponential is ill-behaved. The analysis is extended to the time/frequency domain using a continuous wavelet transform (CWT) [8]. Once in the time/frequency domain, distributions of lifelengths can be calculated at any frequency providing additional insight into the coherent structure phenomena. The event lifetimes, as derived from the corresponding lifelengths, are plotted in the time/frequency domain and called lifetime maps. The lifetime maps are feature rich and exhibit pronounced activity in concentrated areas and no activity in others, a behavior reminiscent of the bursting phenomena described by other researchers [1,2]. The results of these analyses are kept as discrete values so that when a particular result, say, in a lifelength distribution, is of interest, the corresponding interval of time data which created the result can be recovered, allowing inspection of the original pressure data.

The discussion begins with a description of the data set. The data were not taken with the subject analysis in mind, and so the analysis was necessarily adapted to the data. The use of the Gaussian distribution is validated by comparing lifelength distributions derived from frequency-averaged cross spectra to Efimtsov's correlation space scale predictions. The interval correlation technique is introduced with two variants, one using the center sensor of the array as a reference, the other using the first principal component as computed from a singular value decomposition (SVD) of the data. The reader may be more familiar with the term proper orthogonal decomposition (POD) which is an expression common in the literature describing an equivalent computation [9]. Typical results obtained in the time/frequency domain are presented and validated by comparing the median lifelength frequency distributions to the cross-spectrum distributions obtained earlier. The paper concludes with example lifetime maps and some brief discussion as to what the features observed in the maps may mean. As mentioned earlier, the primary focus in this paper is to validate the approach. More work remains to be done to adequately explain the behavior displayed in the lifetime maps.

II. Data Set

The data set was taken aboard a Tupolev Tu-144 as part of NASA's High-Speed Research (HSR) program [10]. Arrays of Kulite XCS-190-15D sensors were installed in window blanks positioned in the forward, center, and aft sections of the aircraft as shown in Fig. 1. The sample rate was 40 kHz in all cases. The analysis was performed on three streamwise Kulites in each window blank as indicated in Fig. 1. The sensor spacing was 6 cm with the exception that the center-to-upstream sensor spacing was 4 cm on the forward and aft window blanks.

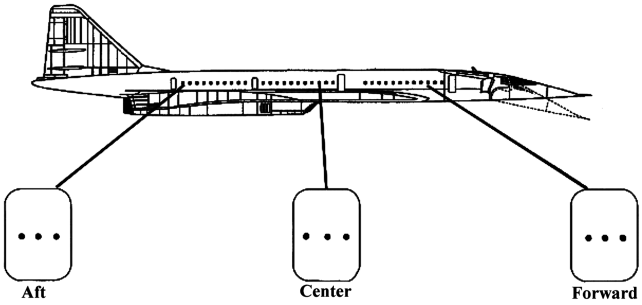

Fig. 1 Sensor layout on Tu-144.

Three flight conditions were available at Mach numbers 0.6, 0.9, and 2.0. Details of each flight condition are listed in Table 1. The freestream velocity U_∞ is computed from the Mach number and speed of sound in air at the indicated altitude. The kinematic viscosity ν is taken from the Aerospaceweb's Atmospheric Properties Calculator[†], which is based on U.S. Standard Atmosphere 1976. The Reynolds number is computed as

$$Re = xU_\infty/\nu \tag{1}$$

The length parameter x is measured from the nose of the aircraft [10]. The coefficient of skin friction C_f, the friction velocity U_τ, and the boundary-layer thickness δ, are computed assuming a one-seventh power velocity profile [11].

$$C_f = 0.0594Re^{-0.2} \tag{2}$$

$$U_\tau = \left(0.5U_\infty^2 C_f\right)^{0.5} \tag{3}$$

$$\delta = 0.382xRe^{-0.2} \tag{4}$$

Note the high Reynolds number in the range of 10^8 for all flight conditions and locations. This may be considered to be just outside the range for which the preceding equations are valid. However, a correction to the boundary-layer thickness for high Reynolds number [10] yields negligible increases except for the Mach 2.0 case, where the correction adds 10%. To maintain consistency for the assumptions used for Eqs. (2–4), it was decided to not add the correction to the boundary-layer thickness and that the 10% error for the one Mach 2.0 case was tolerable.

The convection velocity U_c was calculated from the delay as indicated by the sensor cross correlation between the furthest separated sensors at each location. For comparison purposes, the common estimate for U_c of $0.7U_\infty$ is also given. These values compare very well except for the $M = 2.0$ forward sensor case. At these speeds, one sample delay (25 μs) is equivalent to 80 m/s and thus contributes to the large error. The boundary-layer thickness δ

Table 1 Flight conditions

M	Altitude, km	c, m/s	U_∞, m/s	ν, m^2/s	C_f	U_τ, m/s	Location	x, from nose, m	U_c, m/s	$0.7U_\infty$, m/s	Re	δ, m
0.6	5	320	192	$2.2e-5$	$1.4e-3$	9.98	forward	18.9	143	134	$1.6e8$	0.16
0.9	9	303	273	$3.2e-5$	$1.4e-3$	14.2	forward	18.9	200	191	$1.6e8$	0.16
0.9	9	303	273	$3.2e-5$	$1.2e-3$	13.5	center	32.6	200	191	$2.8e8$	0.25
0.9	9	303	273	$3.2e-5$	$1.1e-3$	12.9	aft	49.3	200	191	$4.2e8$	0.35
2.0	16.9	295	590	$9.8e-5$	$1.5e-3$	31.8	forward	18.9	500	413	$1.1e8$	0.18

[†]http://www.aerospaceweb.org/design/scripts/atmosphere

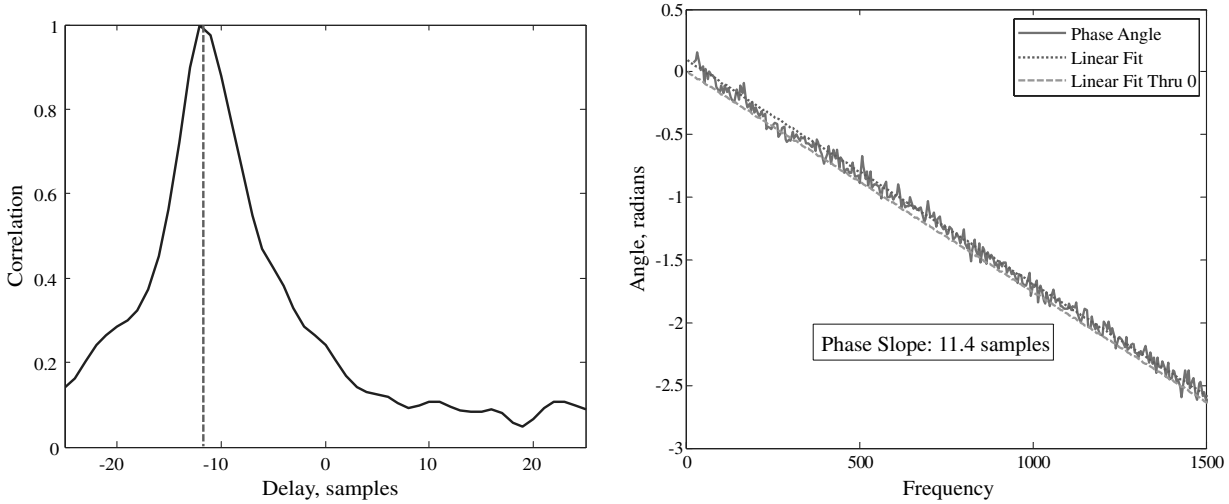

a) b)

Fig. 2 Center section sensors 2 and 3 at $M = 0.9$: a) cross correlation and b) cross-spectrum delay.

ranges from 16 cm for the $M = 0.6$ forward sensor case to 35 cm for the $M = 0.9$ aft sensor case.

Results derived from two sets of data will be presented. The first is taken from the forward sensor set at the three Mach numbers. The second, at $M = 0.9$, is taken from the three different locations. This results in a total of five data sets as shown in Table 1. As previously discussed, the convection delay may have considerable error at high Mach numbers. However this is not the only source of error, as will be discussed next.

The data were analyzed using an interval correlation technique described in Sec. IV and in [3]. The analysis applies an estimated convection delay to the time data to emphasize correlated content. This approach depends on the assumption that the convection delay is constant both over time and frequency. Experience with this data set and others has shown the former assumption to be adequate for the purposes of the subject analysis, however, the latter assumption has been found to cause considerable error under some conditions.

Figure 2 illustrates a best-case example. Here, the convection delay is computed between the second and third center section sensors at $M = 0.9$ using both cross correlation and cross spectrum. That data set consisted of 200,000 samples. An ensemble size of 4000 was used with no windowing, yielding 50 averages with a 10 Hz bin width. The peak delay of 11–12 samples in the cross correlation (Fig. 2a) is shown to compare favorably with the delay as derived from the phase angle of the cross spectrum (Fig. 2b). The linear fit derived from the phase data (dotted line) produces a positive y intercept. At low frequencies, the delay associated with this small phase error will be considerable as shown in Fig. 4a, where the delay appears to diverge from ∼11 samples at approximately 400 Hz.

In contrast, the phase angle, as computed from the same center section at $M = 0.9$ but using the first and second sensors, is shown to begin to depart from the linear fit below 500 Hz (Fig. 3b). Even though the cross-correlation graph in Fig. 3a appears normal, the cross-spectrum phase delay in Fig. 4b reduces to 10 samples at 1250 Hz and then begins to oscillate at 1000 Hz before diverging at 700 Hz. Again, it should be noted that the data used for sensor 2 in Fig. 3 are identical to the data used for sensor 2 in Fig. 2. The error cannot be attributed to sensor phase error as calibration data show phase error to be less than 0.01 rad below 100 Hz. The effect of sensor flushness was evaluated in wind-tunnel tests [10,12], in which the Kulite sensors were installed at varying heights (± 100 μm) and compared with a flush-mounted condenser microphone. The results were tabulated in amplitude deviation ($\pm$dB) over one-third octave bands. The largest amplitude deviations were found to occur below band 30 (1000 Hz). Unfortunately, the effect of sensor flushness on phase accuracy was not reported. Similar amplitude deviations are seen to occur over the same frequency range as the phase errors in the flight data, indicating that sensor flushness may be the underlying

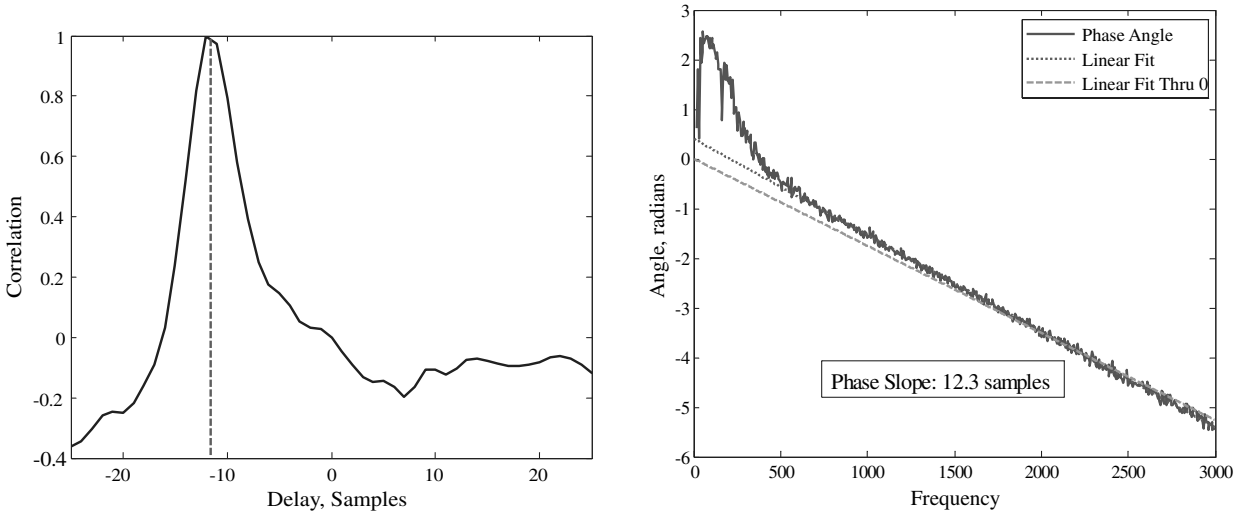

a) b)

Fig. 3 Center sensors 1 and 2 at $M = 0.9$: a) cross correlation and b) cross-spectrum delay.

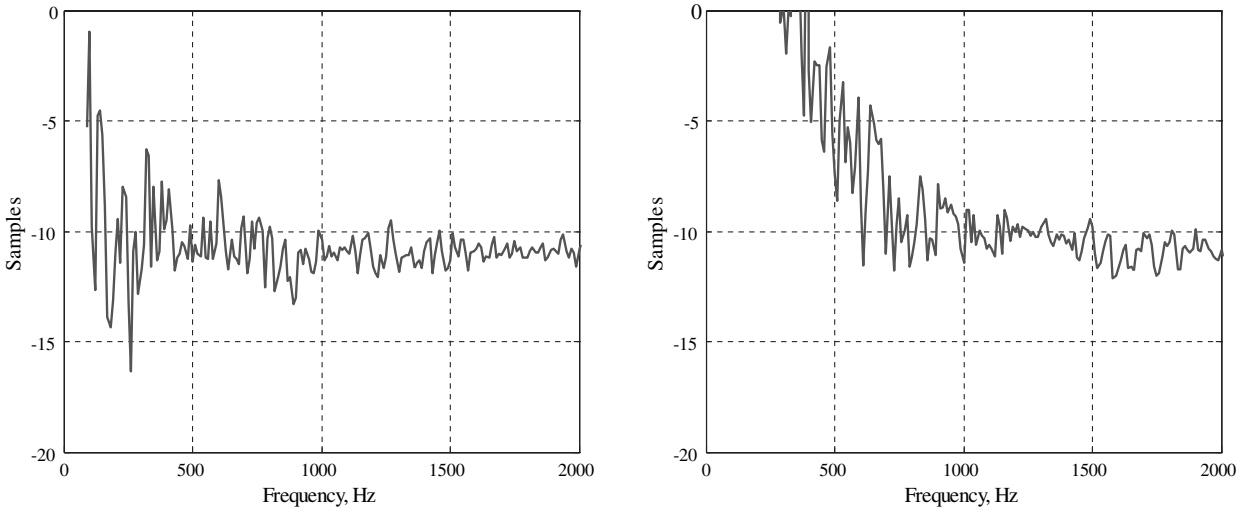

Fig. 4 Comparison of delays calculated from phase angle between a) sensors 2 and 3, and b) sensors 1 and 2.

mechanism for the error observed. As the analysis depends on an accurate estimate of convection delay, an effect on the analysis will be observed and noted where applicable.

Phase-delay divergence can be found in all the data. For example, the data in Fig. 2b may be said to diverge at 400 Hz. Defining the point of divergence as a cutoff frequency for the analysis, the sensor pairs and related cutoff frequencies are listed in Table 2. Four of the 15 sensor pairs in the five selected cases have cutoffs above 500 Hz, the worst case being forward sensor pairs 1 and 3 at $M = 2.0$ with a cutoff at 1200 Hz. The impact of this behavior will be noted where applicable.

III. Correlation Space Scale

Efimtsov [7] defines a correlation space scale Λ as the integral of the normalized cross spectrum φ in the streamwise direction, as given in Eq. (5).

$$\Lambda = \int_0^\infty |\varphi(x, 0, \omega)| \, \mathrm{d}x \tag{5}$$

Computing this integral over the short distance covered by the three sensors on each window blank would not provide a meaningful result. Fortunately, Efimtsov has derived a general form for Λ based on the Strouhal number.

$$\Lambda = \delta \left\{ \left[\left(\frac{0.1Sr}{U_c/U_\tau} \right)^2 + \frac{72.8^2}{Sr^2 + (72.8/1.54)^2} \right]^{-1/2} \right\} \tag{6}$$

where

$$Sr = \omega\delta/U_\tau \tag{7}$$

Sr is the Strouhal number, U_∞ is the freestream velocity, U_c is convection velocity, and U_τ is the friction velocity. The use of Eq. (6) implies that the local flow is aligned in the freestream direction. This may not be the case on an aircraft and will introduce error in the computation of the correlation space scale (as well as the interval correlation described in Sec. IV). Off-axis sensors may be used to quantify the presence of crossflow. Rackl and Weston [12] analyzed the cross spectra of the available off-axis sensors and found the quantities to be in satisfactory agreement with prediction. Although this provides support for the assumption that the effect of crossflow was negligible, it is certain that some crossflow occurred and introduced an unknown amount of error in the analysis. The correlation space scales for the five selected cases were computed using the flight parameters from Table 1 and are shown in Fig. 5. In general, the frequency at which the peak in correlation length occurs is seen to increase with Mach number (Fig. 5a) and decrease with streamwise distance (Fig. 5b).

Table 2 Phase-cutoff frequencies (noted cases are in bold)

Mach	Location	1 > 2 cutoff, Hz	2 > 3 cutoff, Hz	1 > 3 cutoff, Hz
0.6	forward	300	300	300
0.9	forward	400	400	400
0.9	center	**700**	400	500
0.9	aft	400	400	400
2.0	forward	**600**	**600**	**1200**

As mentioned before, direct computation of the integral in Eq. (5) using the data acquired from the small arrays would be impractical. An alternative approach is taken in which a characteristic lifelength λ is defined and optimized to fit a distribution to the sensor cross spectra referenced to the center sensor. The Gaussian distribution is preferred to the pure exponential ($e^{x/\lambda}$) because the analysis is performed on an interval bounding zero where the exponential is ill-behaved. The Gaussian also represents a better model for the coherent structures that the technique is designed to detect, as it supports the assumption that the structures grow, live for a finite time, and then decay. Referencing the center sensor ensures a magnitude peak over the center of the array and is key in locating coherent structure when the technique is extended to the time domain. The form of the estimated cross-spectrum distribution is shown in Eq. (8).

$$\hat{\varphi} = e^{-(x/\lambda)^2} \tag{8}$$

The characteristic lifelength at each frequency is found by applying a least-squares fit of the Gaussian distribution to the cross-spectrum data. This produces a different shaped distribution than the exponential and a reduced value of length scale (discussed in more detail later). Example results obtained from the forward, Mach 0.6 case at 340 Hz are shown in Fig. 6.

$$\hat{\Lambda} = \int_{-\infty}^{\infty} \hat{\varphi}(x, 0, \lambda, \omega) \, \mathrm{d}x \tag{9}$$

$$\hat{\Lambda} = \lambda\sqrt{\pi} \tag{10}$$

The integral of the estimated cross-spectrum distribution, Eq. (9), conveniently evaluates to $\lambda\sqrt{\pi}$, Eq. (10). The estimated correlation space scale $\hat{\Lambda}$ will be referred to as the lifelength for the remainder of the paper.

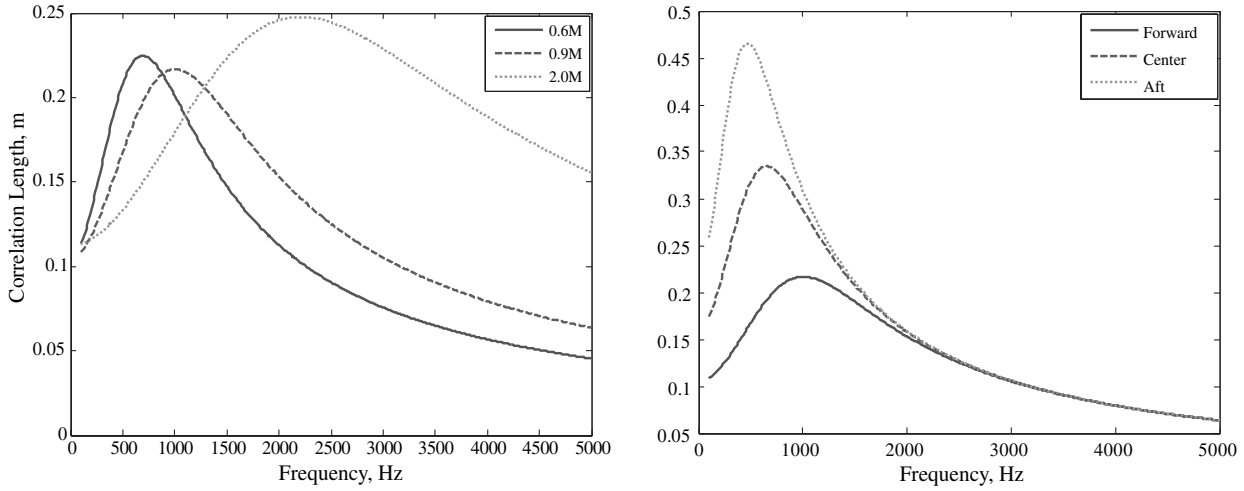

Fig. 5 Correlation space scales for three Mach numbers at a) forward location and b) three locations at $M = 0.9$.

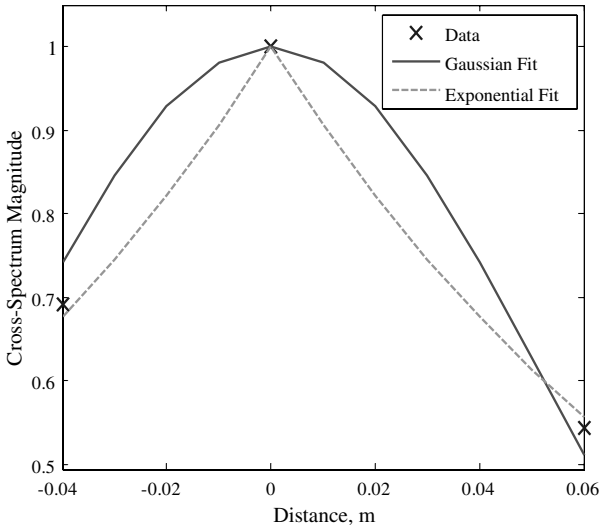

Fig. 6 Center referenced cross spectrum, Gaussian fit, exponential fit, forward location, Mach 0.6, 340 Hz.

If it were desired to use the classically defined correlation length [6], a two-sided exponential distribution could be defined, for example, by taking the absolute value of the exponent rather than the square. The estimated correlation space scale would then be 2λ, very close to the 1.77λ returned by the Gaussian. The downside of using the exponential is that the distribution produces a singularity at zero and is thought to be an unnatural fit for the kind of behavior expected of coherent structures, although, with only three sensors, the true distribution cannot be observed.

In Figs. 7a–7c, the predicted correlation space scale for a two-sided distribution 2Λ is compared with the measured exponential and Gaussian fits for the forward sensor cases. The exponential fit should match the predicted correlation space scale better than the Gaussian. In general, the Gaussian fit should be expected to return a smaller length scale than the exponential fit for the same data. The $M = 0.9$ exponential fit (Fig. 7b) agrees well with predictions attaining a peak of about 45 cm at 750 Hz vs the predicted 47 cm at about 1 kHz. The measured $M = 0.6$ (Fig. 7a) cases have broad peaks from 500 to 750 Hz. The exponential fit peaks at 24 cm. This is the correct frequency range, but lower than the 47 cm predicted. The measured $M = 2.0$ exponential fit (Fig. 7c) peaks at 27 cm, which is substantially lower in magnitude than the predicted case at 53 cm. It should be noted that this case was marked in Table 2 as having a high cutoff frequency and, therefore, could be expected to return questionable results.

Figure 8 compares the $M = 0.9$ cases. Here, the forward case is the same as the forward $M = 0.9$ case in Fig. 7b. The aft exponential fit Fig. 8b peaks at the predicted frequency, but at a higher value, 150 vs 110 cm. The center exponential fit (Fig. 8a) compares poorly with the prediction exhibiting no peak and attaining a maximum value less than 20 cm vs the nearly 75 cm predicted. Again, the cutoff frequency at 700 Hz for this case may be interfering with the analysis, as it occurs very near the predicted peak.

The estimated correlation space scale, computed using a Gaussian fit, has been shown to be less sensitive to length scale, consistently returning measures lower than the exponential fit. This can be understood by comparing the distribution shapes in Fig. 6. To fit data representing long correlation lengths, the exponential must return a larger characteristic length than the Gaussian. In the example shown in Fig. 6, the exponential characteristic length is 10 cm, whereas the Gaussian is 7.3 cm. For longer length scales, as represented by the aft, $M = 0.9$ case in Fig. 8b, the difference between the two distributions becomes considerable, the exponential requiring much larger characteristic lengths to fit the same data. This is why the Gaussian is thought to be a more natural fit for coherent structures that are expected to have longer length scales. Although less sensitive than the exponential, the Gaussian distribution captures relevant behavior and can be used as an effective measure. The technique is applied to time domain data using interval correlation as explained in the next section.

IV. Time Domain

To locate coherent structure in the turbulent boundary-layer time data, intervals are found in which a coherent structure is suspected to have occurred. Assuming that coherent structures have long lifelengths, this would involve scanning the data sets for time intervals in which long lifelengths are detected. Two techniques have been developed for this purpose. Both techniques use an interval correlation function, Eq. (11), on data taken from a subset, or window, in the time history of length n. One technique uses the center sensor as a reference, the other a value derived from a SVD of the data.

$$ic_{r,2,i} = \frac{\mathbf{td}_i \cdot \mathbf{td}_r}{\left(\mathbf{td}_r^2\right)^{0.5}\left(\mathbf{td}_2^2\right)^{0.5}} \tag{11}$$

Here, the time data from channel i is delayed or advanced with respect to the center sensor according to estimates of the convection velocity and sensor separation, Table 1. The summed product of the time data and the reference data are normalized by the root mean square of the reference data $\mathbf{td}_r$ and the center sensor data $\mathbf{td}_2$. Using

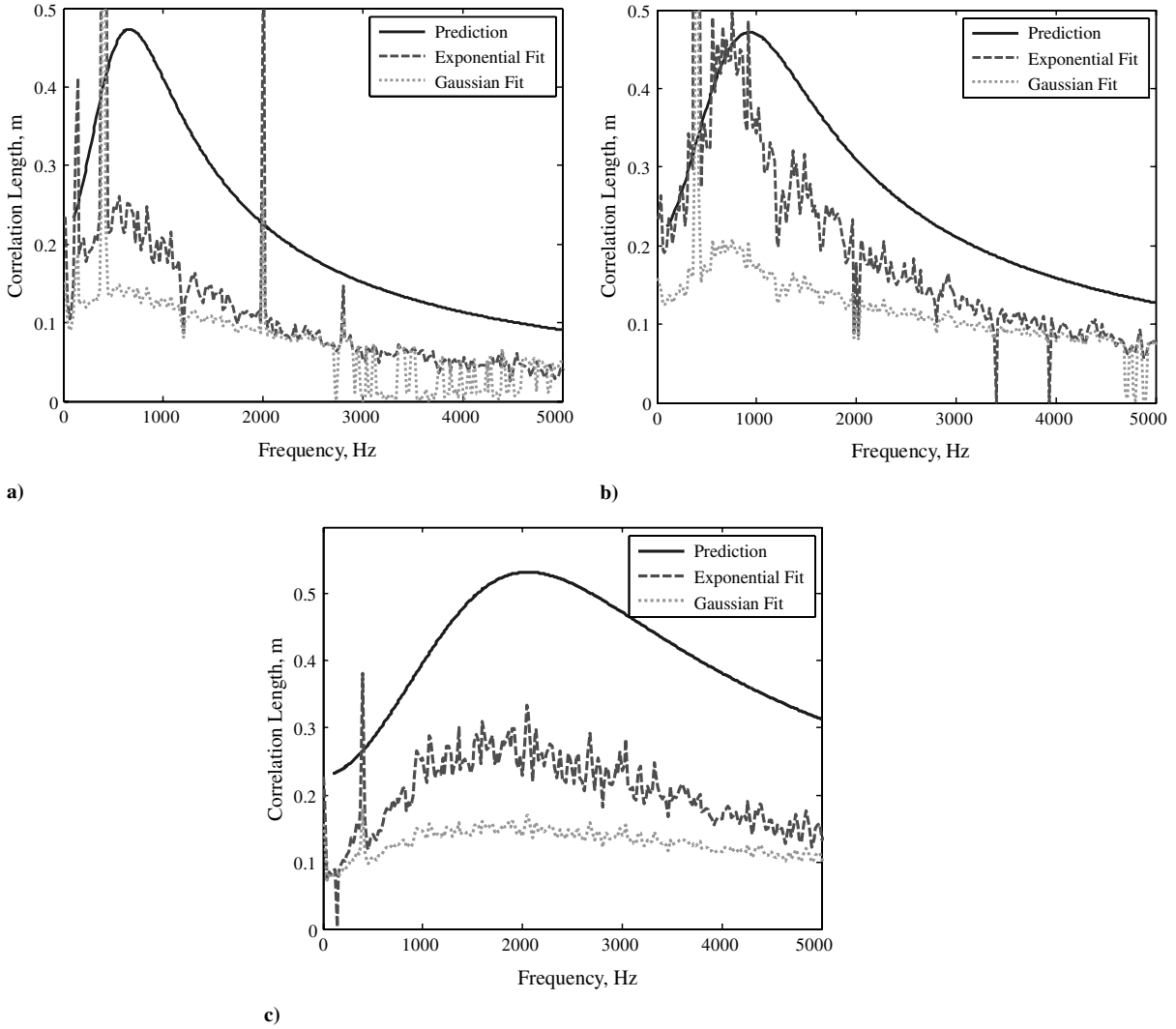

Fig. 7 Comparison of predicted correlation space scale to lifelength for forward cases: a) $M = 0.6$, b) $M = 0.9$, and c) $M = 2.0$.

the center sensor to normalize the interval correlation was useful in rejecting degenerate solutions in SVD referenced analyses where, in the case in which little correlation exists, the rms value of the SVD reference can become very small, inflating the results. The details of the analyses will be described next and compared in Sec. V.F.

A. Center and Principal Component Referenced Analysis

Center referenced (CR) analysis is performed using the center channel time data as the reference, i.e., with $r = 2$ in Eq. (11). This type of analysis has the benefit of automatically normalizing the center data point to one, thus reducing the chance of false detections

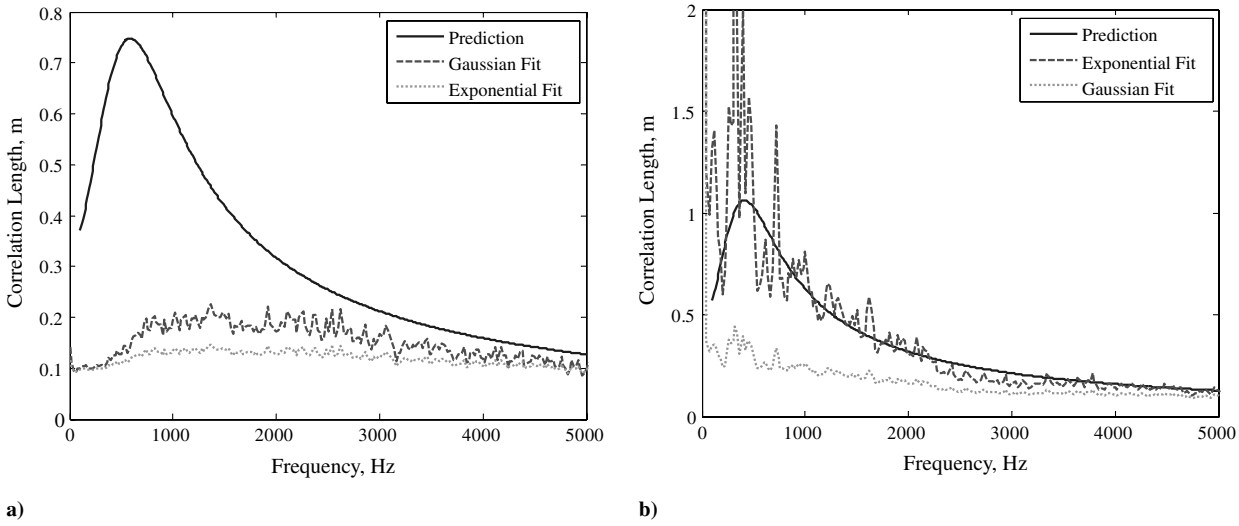

Fig. 8 Comparison of predicted correlation and measured space scale to lifelength for $M = 0.9$ cases: a) center and b) aft.

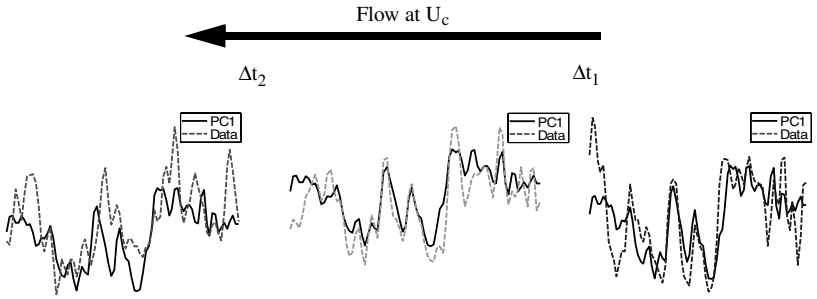

Fig. 9 Time-delayed pressure data compared with first principal component.

as might happen using the principal component analysis as described next.

Singular value decomposition is also referred to as principal component analysis (PCA) and may be best known as proper orthogonal decomposition in the area of turbulence study [2]. The objective is to extract the most correlated behavior from the sensor data. The SVD algorithm [13] decomposes the time-delayed data into a diagonal matrix of singular values **S**, and left and right unitary matrices **U** and **V**, respectively. The first singular value is then used to construct the first principal component, or first mode, of the data.

$$\mathbf{TD} = \begin{bmatrix} td_{11} & \cdots & td_{1n} \\ \cdots & \cdots & \cdots \\ td_{m1} & \cdots & td_{mn} \end{bmatrix} \tag{12}$$

$$\mathbf{TD} = \mathbf{U} \times \mathbf{S} \times \mathbf{V}^H \tag{13}$$

$$\mathrm{PC}_1 = \mathbf{U} \times \begin{bmatrix} S_{11} & \cdots \\ \cdots & \cdots \end{bmatrix} \times \mathbf{V}^H \tag{14}$$

$$\mathrm{ic}_{\mathrm{PC}_1,2,i} = \frac{\mathrm{PC}_1 \cdot \mathbf{td_i}}{\left(\mathrm{PC}_1^2\right)^{0.5}\left(\mathbf{td_2^2}\right)^{0.5}} \tag{15}$$

The time-delayed data $\mathbf{td_i}$, consisting of n samples from m sensors, are formed into a matrix **TD**, as shown in Eq. (12). The SVD algorithm returns matrices **U**, **S**, and **V** such that **TD** can be reconstructed as in Eq. (13), where H denotes the complex transpose. The first principal component $\mathbf{PC_1}$ is formed by using only the first singular value S_{11}, with the matrices **U** and **V** as shown in Eq. (14). The PC-referenced interval correlation can then be formed as in Eq. (15).

An example comparing the first principal component to the data from which it was derived is shown in Fig. 9. Note that the SVD does a very good job in constructing a wave shape that has a lot in common with its parent data. A very real problem exists with using this kind of decomposition with so few sensors in that correlation is found where none really exists. This will be discussed in more detail after the time/frequency domain analysis is introduced in Sec. V.F.

B. Gathering Statistics

Lifelength statistics can be computed in the time domain by replacing the cross spectrum with the interval correlation function. Using the interval correlation function on a series of subintervals of the data set, a number of samples can be collected characterizing the lifelength distribution of the data. Figure 10 shows a typical result for the forward sensor $M = 0.6$ case taken with an interval size of 100 samples. The distribution is characterized by its median, maximum, and 75th percentile values. These values for the selected cases are shown in Table 3, where the cases with high cutoff frequencies are in bold. The results are in line with the cross-spectrum values, although it is difficult to make a comparison because the time domain result is

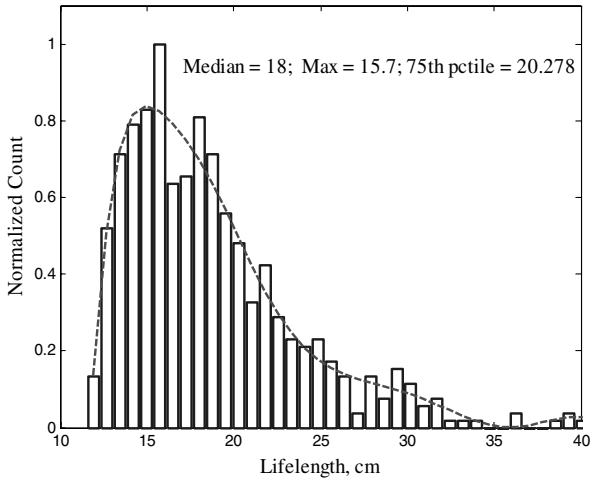

Fig. 10 Lifelength distribution taken from forward, $M = 0.6$ case.

an average over all frequencies. The time domain analysis has another drawback in that the selection of an analysis interval skews the results with large intervals, masking high frequencies and short intervals being biased by low frequencies. This problem is avoided by performing the analysis in the time/frequency domain as will be discussed next.

V. Time/Frequency Domain

The time data can be transformed to the time/frequency domain using a continuous wavelet transform (CWT). See Farge [14] for an introduction to the topic. The Morlet wavelet, one of many wavelet functions, was chosen as a basis for the transformation because it matched the form of observed long-life phenomena [3]. The Morlet wavelet is defined in Eq. (16).

$$\Psi_{\mathrm{Mor}}(t) = \frac{1}{\sqrt{f_b \pi}} e^{i2\pi f_c t} e^{-t^2/f_b} \tag{16}$$

The Morlet wavelet is characterized by two parameters, the wavelet center frequency f_c and the envelope shape f_b. An example wavelet with $f_b = 1.5$ and $f_c = 1.0$ is shown in Fig. 11.

Table 3 Time domain lifelength statistics

Case	Maximum, cm	Median, cm	75th percentile, cm
$M = 0.6$, forward	16	18	20
$M = 0.9$, forward	15	18	22
$M = 0.9$, center	17	18	21
$M = 0.9$, aft	19	21	25
$M = 2.0$, forward	14	18	21

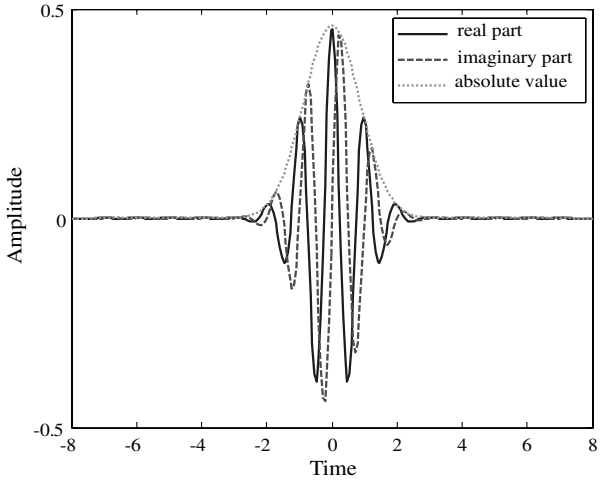

Fig. 11 Morlet wavelet for $f_b = 1.5$ and $f_c = 1.0$.

A wavelet is applied to a signal by convolution, e.g.,

$$W(t') = \int s(t)\Psi(t - t')\,\mathrm{d}t \tag{17}$$

where $s(t)$ is the signal and Ψ is the wavelet function. This will return a filtered signal for the particular wavelet applied. To form a continuous wavelet transform, the wavelet is scaled so that its center frequency is varied over the frequency range of interest.

$$C(a, t') = \int s(t)\frac{1}{\sqrt{a}}\Psi\left(\frac{t - t'}{a}\right)\mathrm{d}t \tag{18}$$

The continuous wavelet transform $C(a, t')$ has frequency F_a, which corresponds to the scale factor a by

$$F_a = \frac{f_c}{a\Delta} \tag{19}$$

where Δ is the signal sample period [8]. The resulting transform has the properties of a time-frequency spectrum as can be illustrated by considering the example of a chirp signal, as shown in Fig. 12a. This chirp varies from 10 Hz to 1 kHz, as is clearly seen in its power spectrum in Fig. 12b.

The continuous wavelet transform of the chirp is shown in Fig. 13a, with the color axis in decibels. One feature that is immediately obvious is the widening of the bin width with frequency. This characteristic results from the pronounced localization of the wavelet as its features are scaled. At higher frequencies, the wavelet envelope narrows, reducing the effective sample interval, thus widening the transformation bin width. Although the Morlet wavelet lacks orthogonality, the shape of the

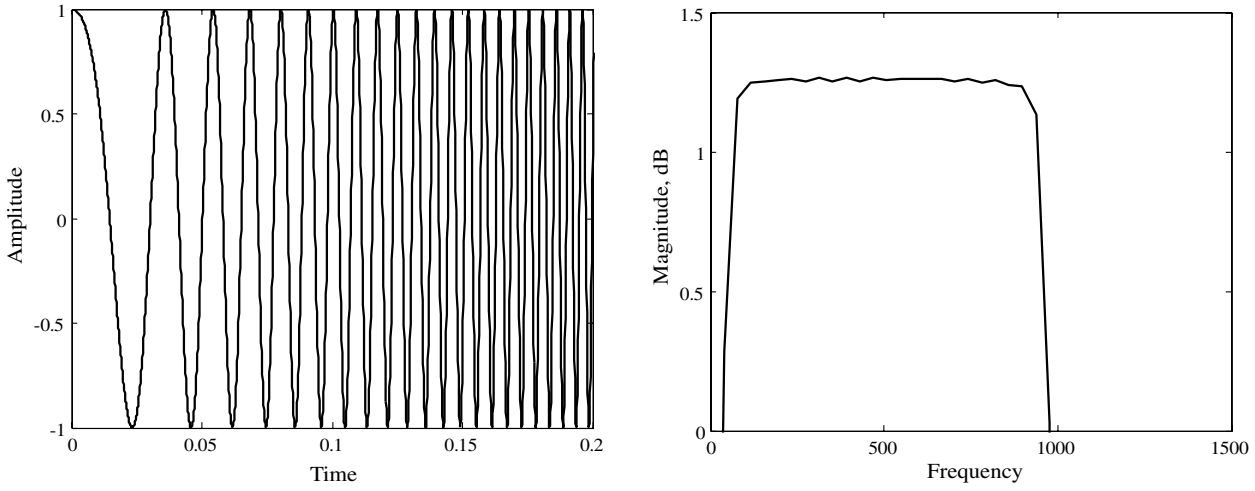

a) **b)**

Fig. 12 Chirp signal: a) time history and b) associated power spectrum.

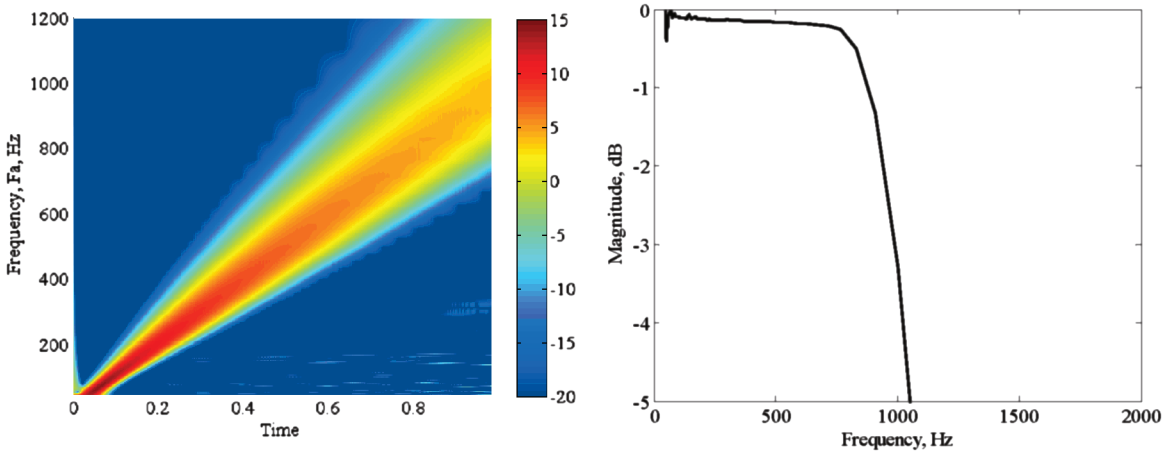

a) **b)**

Fig. 13 Chirp signal: a) continuous wavelet transform and b) power spectrum derived from CWT.

power spectrum is well maintained, as shown in Fig. 13b where the summed transform is plotted.

A. Continuous Wavelet Transform of TBL Data

Applying a continuous Morlet transform to an interval of time data (as shown in Fig. 14a), produces the time-frequency spectrum shown in Fig. 14b, in which the absolute magnitude of the complex transform is plotted. The wavelet transform is able to highlight structures which may be of interest and provide estimates of their approximate frequency content and power. As found with the chirp data, the shape of the power spectrum is maintained, Fig. 14c, although the absolute magnitude is not. More details on the procedure used to create the CWT can be found in [3]. Once in the time/frequency domain, interval correlations can be done at each frequency, i.e., each row of data in the CWT. However, here, the real part of the complex wavelet transform is used to provide the phasing information necessary for the interval correlation computation. Besides the ability to view the frequency distribution of the lifelength statistics, this approach offers the ability to size the analysis subinterval to a number of periods, thus varying the subinterval size with frequency and removing the bias a constant subinterval introduces. The following sections are largely dedicated to validating this approach, identifying its pitfalls, and recommending improvements.

B. Lifelength Frequency Distribution

The lifelength frequency distribution for the forward $M = 0.6$ case is shown in Fig. 15a with the distribution's median and 95th percentile in Fig. 15b. In Fig. 15a, the color in the plots relates to the number of events, with red being highest. It can be seen that, as the distribution broadens at lower frequencies, fewer events occur along the median value. A related effect is that, as more of the events occur at larger lifelengths, fewer events will occur in general.

C. Comparing Interval Correlation to Cross-Spectrum Results

The median lines from the lifelength frequency distributions of the forward sensor cases are plotted in Fig. 16, along with the cross-spectrum results taken from Fig. 7. Excellent agreement is obtained between these two very different techniques. The lifelength derived from the $M = 0.9$ case, in Fig. 16b, peaks at a lower frequency (400 Hz) than the cross-spectrum result (700 Hz), reemphasizing a trend away from the Efimtsov prediction showing a peak at 1000 Hz, Fig. 7b. The $M = 0.6$ case, Fig. 16a, shows a similar trend, indicating a peak in the median at a lower frequency than predicted. The $M = 2.0$ case in Fig. 16c follows the cross-spectrum results very closely. All cases in Fig. 16 exhibit an abrupt dropoff below 400 Hz. This is most likely due to errors in the phase delay at low frequencies as described earlier (Sec. II).

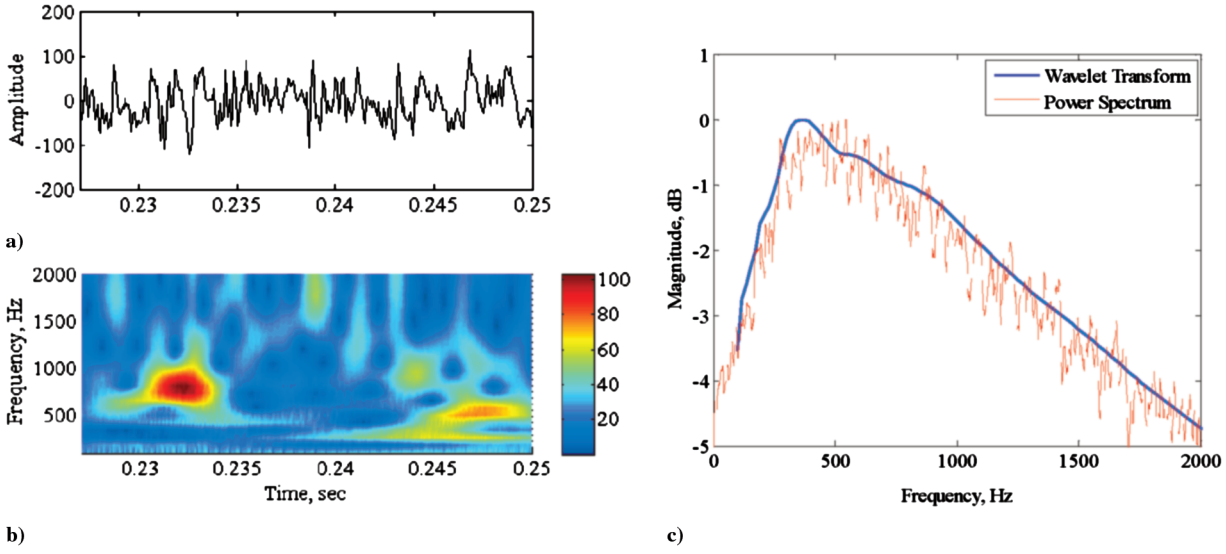

Fig. 14 TBL data: a) time history, b) associated continuous wavelet transform, and c) power spectrum compared with summed wavelet transform.

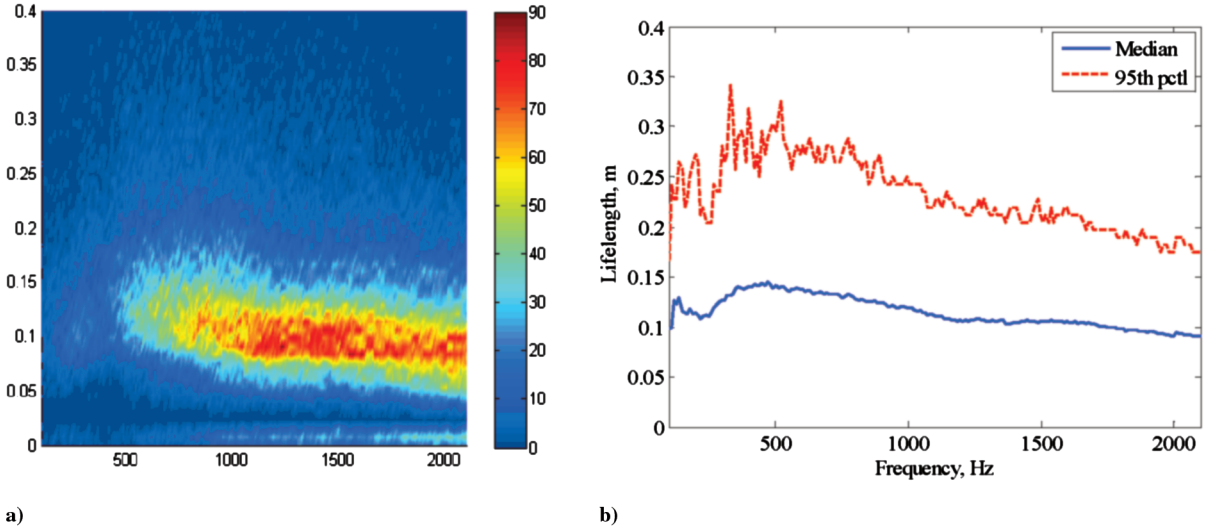

Fig. 15 Forward sensor $M = 0.6$ case: a) lifelength frequency distribution (color indicates number of events), and b) related median and 95th percentile.

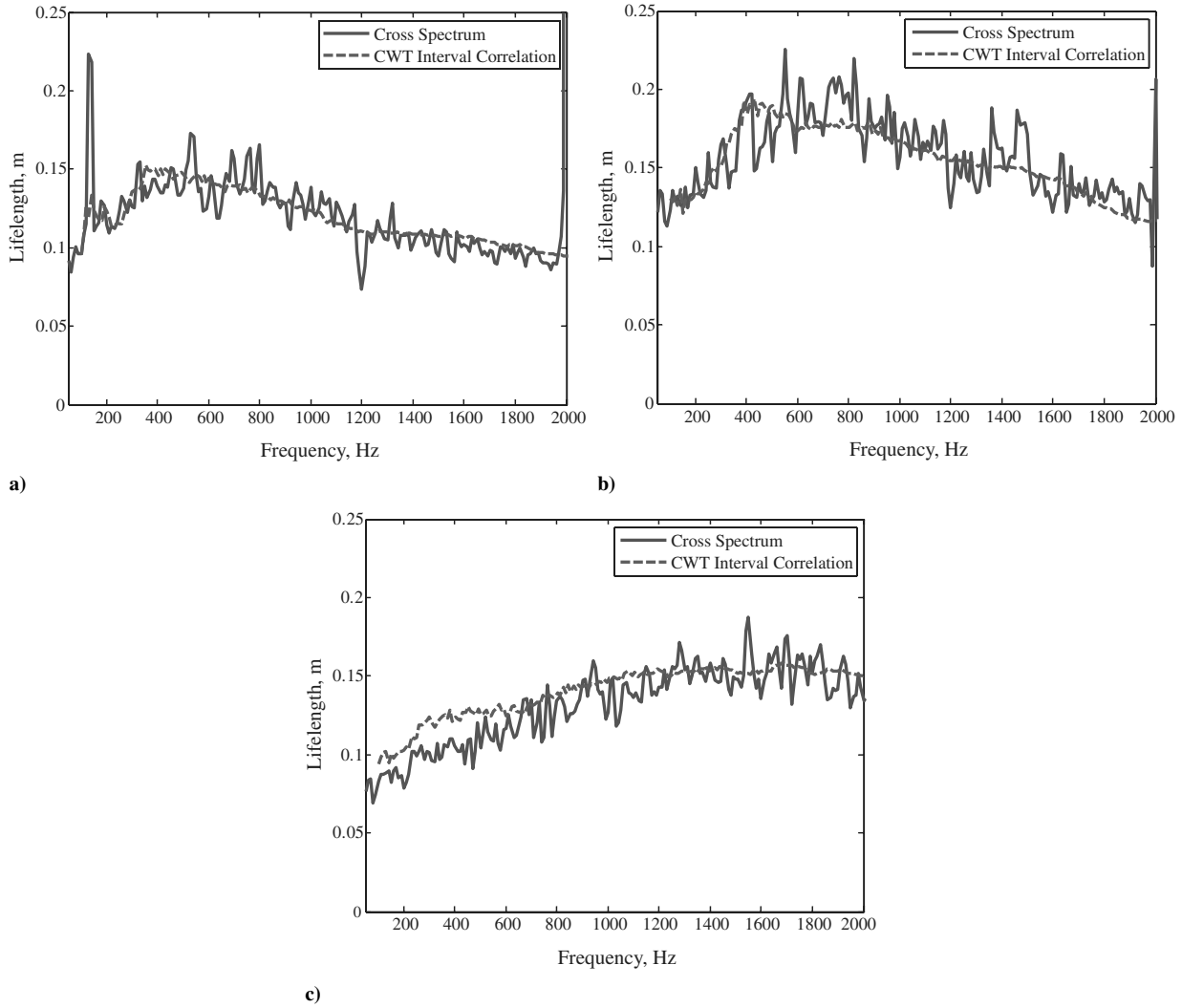

Fig. 16 Median lifelengths from CWT analysis compared with lifelength estimates from cross spectrum for the forward sensor cases: a) $M = 0.6$, b) $M = 0.9$, and c) $M = 2.0$.

The medians of the lifelength frequency distributions for the $M = 0.9$ cases are shown in Fig. 17. One immediately apparent difference in the results is seen for the aft sensor case, Fig. 17b, in which the interval correlation result below 400 Hz does not return lifelengths as large as those indicated by the cross-spectrum results. The error again seems to be related to the departure of the phase delay at the lowest frequencies from the practically constant value observed at mid to high frequencies.

D. Comparing Wavelet Transform Data to Time Domain Data

Once a subinterval with large lifelength has been located, the original time data can be retrieved. For the purposes here, this is done

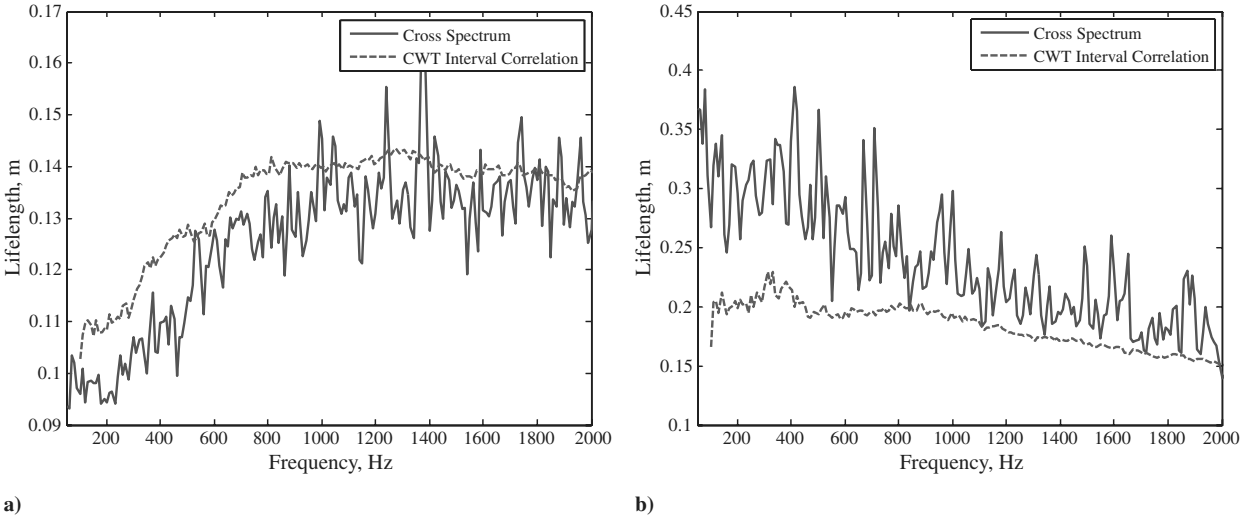

Fig. 17 Median lifelengths from CWT analysis compared with lifelength estimates from cross spectrum for $M = 0.9$ cases: a) center, and b) aft.

to increase confidence in the analysis. In future analyses, this can be done to increase understanding of the physical phenomena.

The lifelength frequency distributions are composed of discrete events. Each dot in Fig. 15a can be queried and the originating data displayed. For example, the CWT in Fig. 18a is associated with an event detected at 331 Hz with a lifelength of 0.75 m for the forward, $M = 0.6$ case. The CWT is three subintervals long with the subject data highlighted in the figure. The data displayed in Fig. 18a are the amplitude of the real part of the CWT. Several features are apparent in the data. One is that there appears to be a continuous tone just below 400 Hz which morphs into the subject event. This feature is 400 Hz noise introduced by the electronics. The noise is rejected by the analysis as it has zero phase delay across the sensor set. However, the noise does obscure the pressure data in the narrow band around 400 Hz. Another feature is the second harmonic at ~660 Hz which appears in the center subinterval. One might wish to know the lifelengths of the features surrounding the detected event. This is addressed in Sec. VI. The actual wavelet filtered data are shown in Fig. 18b. The high degree correlation in the three sensors which led to the long lifetime is obvious. To test whether this is real or somehow a result of the analysis, we look to the original time data.

The delayed time data associated with the graphs in Fig. 18 are shown in Fig. 19a. The presence of a persistent low frequency can be seen in the data with a more pronounced feature centered in the detected subinterval.

The bandpass filtered time data is shown in Fig. 19b. The filter is centered at 331 Hz with a bandwidth of 200 Hz. This is wide compared with the 10 Hz bin width of the CWT, but similarities can be seen in the data, i.e., comparing Fig. 19b with Fig. 18b. Notice, for example, that between 4 and 8 ms, the red curve has higher amplitude and is leading, and the green curve is of lower amplitude and lagging in both figures. Also note between 16 and 18 ms that the relative amplitude and phase of the three signals are almost identical in the two figures. These kinds of comparisons improve with narrower filter bandwidth and have been found to be consistent throughout the test cases. This raises confidence in the technique to a high level, encouraging further analysis and insight. For example, note that the bandpass filtered data are shown to have 33% of the rms power contained in the original data. One percent of the bandwidth contains 33% of the power. This indicates that coherent structures do contain a lot of power relative to less correlated phenomena.

E. Event Detection Rate

Degenerate events are rejected by the analysis. See Sec. V.F for an explanation on why and how this is done. It is also possible that nonlinearities in the flow, such as a change in frequency content as the feature propagates, would defeat the analysis, thus events are not detected in every sample interval. An event detection rate can be obtained by the ratio of the total number of events successfully detected to the total number of intervals sampled. This figure is not an

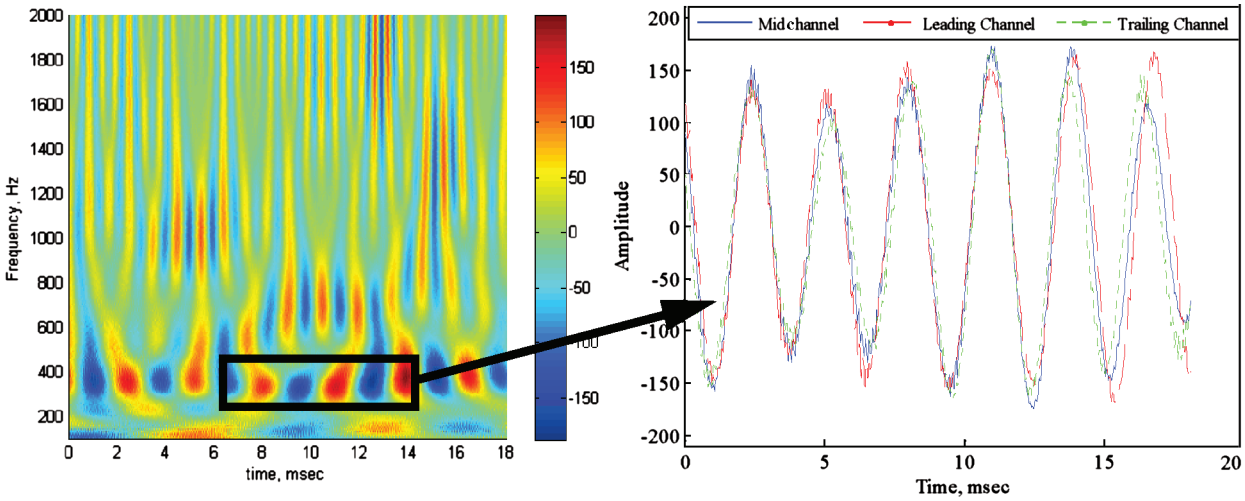

Fig. 18 Data taken from selected time interval: a) CWT and b) at 331 Hz.

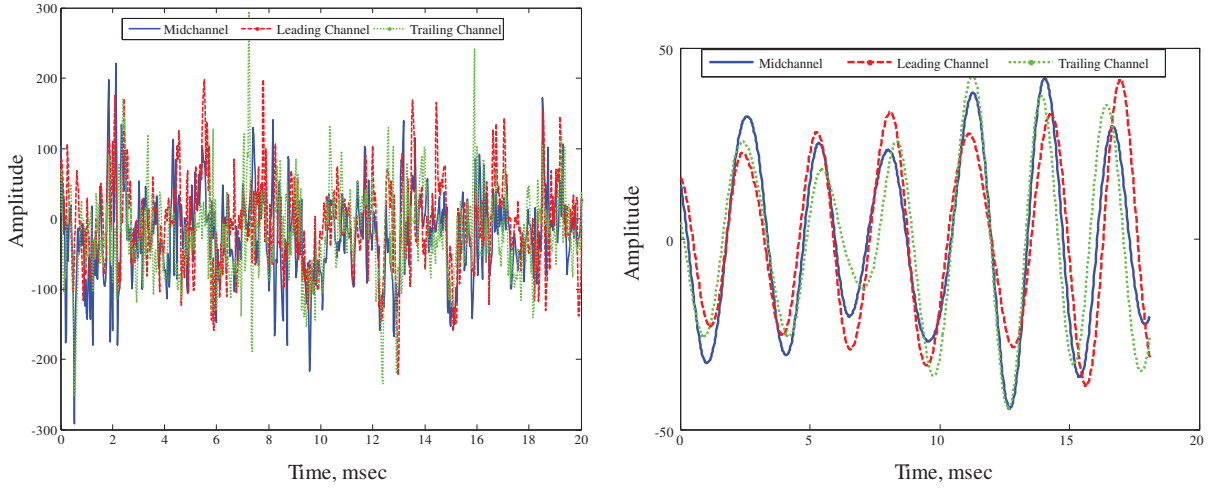

Fig. 19 Time history data: a) original, and b) result of 200 Hz bandpass filter.

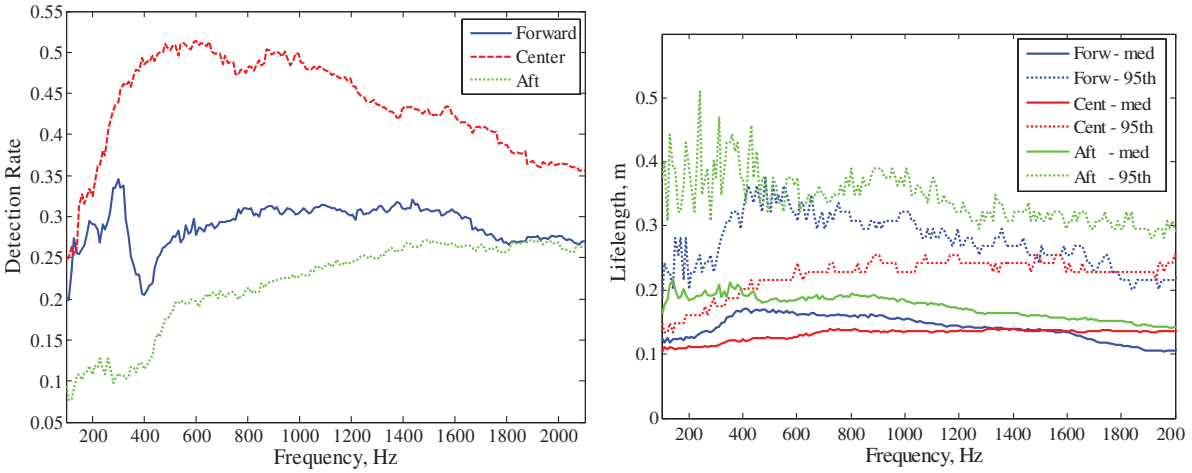

a) b)

Fig. 20 $M = 0.9$ cases: a) detection rate, and b) lifelength median and 95th percentiles.

estimate of how often an event occurs, but how often it is detected. The difference here is that if the sample interval is significantly smaller than the feature size, the event will be detected several times, thus increasing the detection rate. This is discussed in more detail in Sec. VI. The detection rates for the $M = 0.9$ cases are shown in Fig. 20a with the corresponding lifelength median and 95th percentile in Fig. 20b. The center section has the highest detection rate and smallest lifelength, whereas the aft section has the lowest rate and largest lifelength. This relationship is as expected in that longer lasting events will occur less often.

F. Comparing Singular Value Decomposition to Center Referenced

The previously presented data are largely from interval analysis using PC_1 referenced interval correlation. The SVD reconstruction is able to generate a shape with the highest correlation among the data sets. The center referenced analysis works with the data as they are, and thus consistently returns lower lifelength values. This effect can be seen in Fig. 21a where the SVD and CR analyses are compared for the forward sensor $M = 0.6$ case.

Note that the two results are very similar, with the exception that the CR results are lower. This brings up the question as to whether the indicated coherent structure is real or serendipitous. Are actual long lifelength features being detected or are they just the accidental overlay of otherwise random events? To test this, both analyses were run on completely random data. The results, Fig. 21b, indicate that the SVD will indeed extract correlated from uncorrelated data. The interval correlation technique is particularly vulnerable in that the first principal component constructed from relatively uncorrelated data sets will not be highly correlated with the center sensor, thus creating a low, flat distribution indicative of a long lifelength. One way to reject these aberrations is to place a lower limit on the power required in the first PC for an event to be considered valid. The CR approach is less susceptible to this effect because using the center sensor as a reference assures a correlation of one at the center of the distribution. In the extreme, i.e., for lifelengths much longer than the median, both approaches will detect events where there should be none, as there is a nonzero probability that the random data would overlay. One reason for this is that this particular data set consists of only three sensors. Increasing the array both in number and length will reduce the likelihood that the random data would correlate and increase the ability of the analysis to reject random events.

VI. Lifetime Maps

The lifelength data derived from the interval correlation analysis can be converted to lifetimes and plotted in the time/frequency domain. The lifelengths are converted using the estimated convection velocity. The resulting lifetime maps can then be conveniently compared to the continuous waveform transform plots. Examples of these plots are shown in Figs. 22–24 for the $M = 0.9$ cases. In the lifetime maps, the color of the indicator is the lifelength, and the length of the indicator in the time direction is the lifetime. The analysis intervals are 4 cycles long and are sampled every 2 ms, so

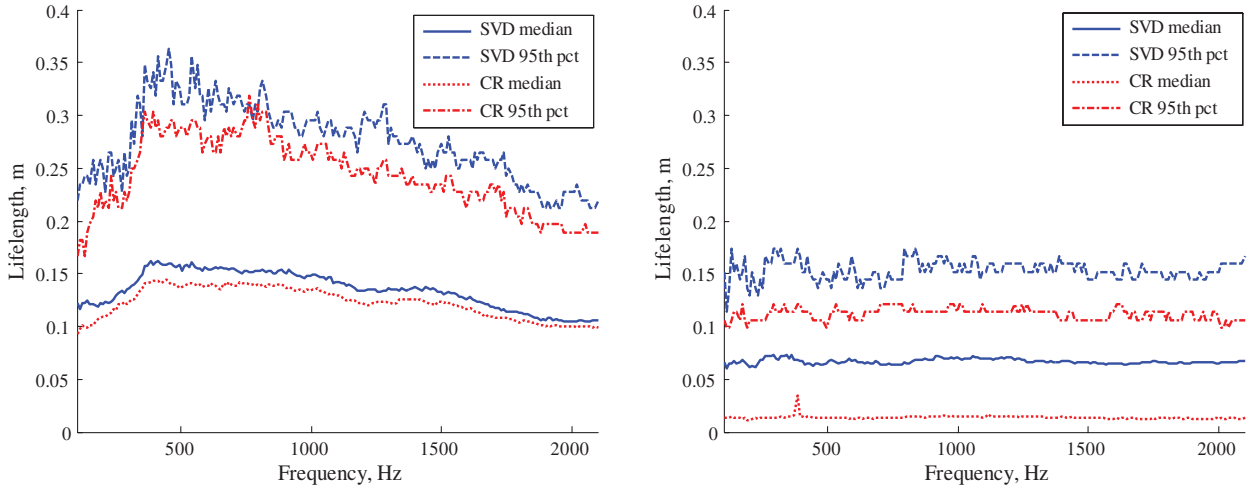

a) b)

Fig. 21 SVD and CR results compared: a) forward sensor $M = 0.6$, and b) random data.

that the samples are continuous at 2000 Hz and overlapped 50% at 1000 Hz. The lifetime map, Fig. 22b, appears to have lines of constant time at high frequencies which bend toward increasing time at low frequencies. This is due to the lifetime indicators being plotted in the center of the analysis interval which increases in size at lower frequencies. This plotting technique was used so that the lifetime indicators would be placed close to the CWT data from which it was derived. Lifetime data derived from the center sensor array are presented first, as it displays clear indicators of behavior which become less obvious in the forward and aft cases.

The dominant feature of the lifetime map of the center sensor in Fig. 22b is the area from 25 to 50 ms and 400 to 600 Hz. This area contains a region of lifetimes which approach the sample period of 2 ms, implying continuous correlated activity. The long-lifetime region corresponds to a feature in the CWT at 35 ms and from 400 to 600 Hz which resembles a flame, having a broad base at low frequency and necking down at higher frequencies, becoming almost wispy above 1000 Hz. These types of features are common in the CWT, but do not always produce long-lifetime indications. The regions to the left and right of the long-lifetime region in Fig. 22b are best described as two ellipsoid regions void of correlated activity, but surrounded by long-lifetime events which delineate the voided regions. It is common to observe the widening and abrupt termination of a lifetime line as it is traced in frequency. Quite often, the line reappears after a small gap, resuming a long-lifetime indication before narrowing down again. Several examples of this kind of behavior can be found in all lifetime maps. The behavior appears to indicate that the data in the voided region are nonlinear, varying in frequency and/or phase as the features propagate, defeating the interval correlation analysis.

The CWT and lifetime map for a sample of data taken from the forward section are shown in Fig. 23. An immediate observation is that the lifetime map of the forward section is less dense than that of the center section. This follows from Fig. 20, which indicates that the center section had the highest detection rate and lowest lifelengths. The majority of the behavior in the center section data appears average, i.e., most of the lifetimes are <1 ms with occasional bursts of longer lifetime behavior. The lifetime map of the forward section data, Fig. 23b, contains larger voided areas than the center section. This would contribute to a lower detection rate, again in agreement with the result plotted in Fig. 20. As in the center section case, the voided areas are surrounded by long-lifetime events, giving the impression that the analysis is failing to detect long-lifetime structures that appear to exist in these regions. A common characteristic found in voided areas can be observed in the CWT in Fig. 23a in the area which corresponds to the voided region from 40 to 75 ms around 400 Hz in the lifetime map in Fig. 23b. Higher amplitude indications exist at the borders of the region in the CWT, where long lifetimes exist in the lifetime map, with the interior, voided, region becoming bifurcated. It is possible that the void is a normal representation of strong bimodal behavior. This kind of modal behavior is in contrast to the long, continuous lifetime lines in

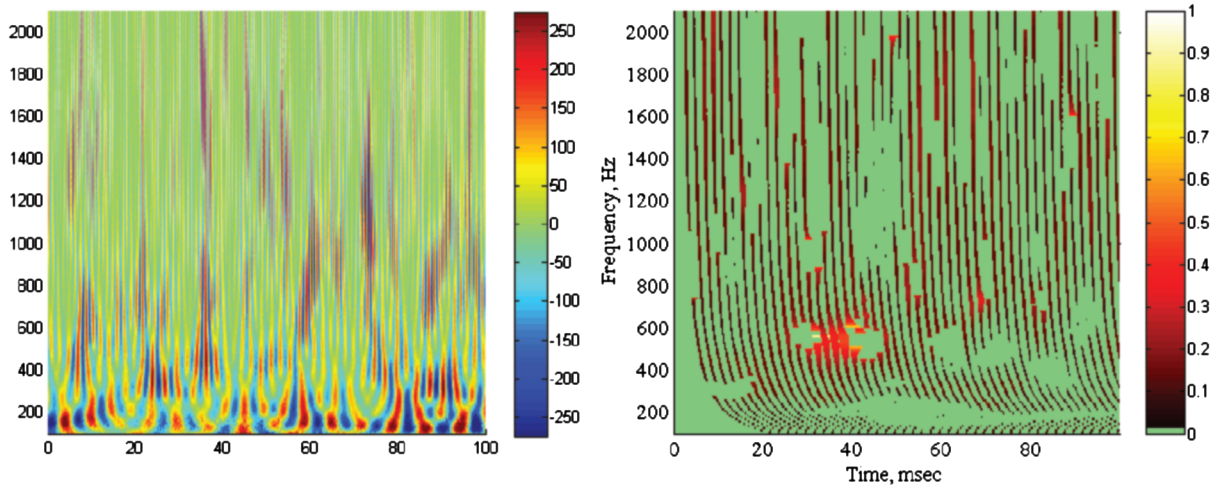

a) b)

Fig. 22 Data taken from center sensor array at $M = 0.9$: a) CWT, and b) lifetime map. Color in Fig. 22b relates to lifelength in meters.

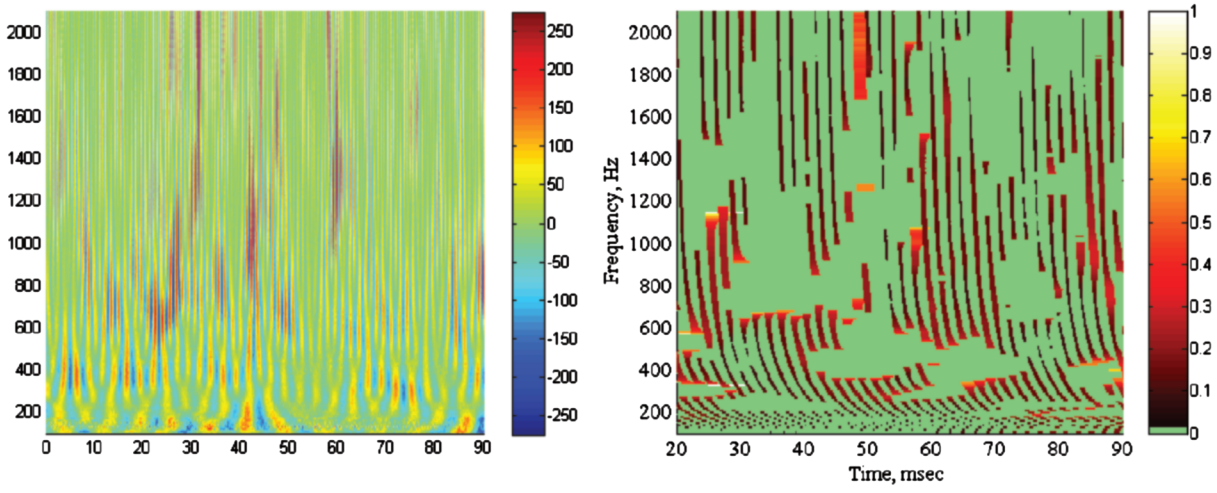

a) b)

Fig. 23 Data taken from forward sensors at $M = 0.9$: a) CWT, and b) lifetime map. Color in Fig. 23b relates to lifelength in meters.

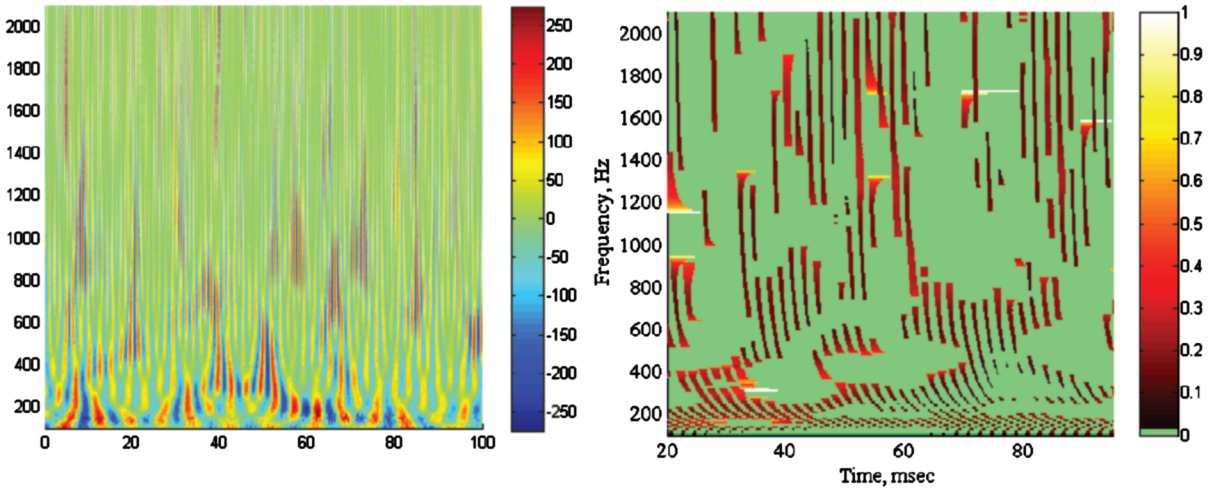

a) b)

Fig. 24 Data taken from aft sensors at $M = 0.9$: a) CWT, and b) lifetime map. Color in Fig. 23b relates to lifelength in meters.

Fig. 22b, which are more indicative of broadband behavior with short lifelengths. It is then the voided areas, including the surrounding long-lifetime borders, which might indicate the presence of a persistent but not necessarily coherent structure. The voided regions are at least 10 ms in duration. This would correspond to a feature length of 2 m, very much larger than the estimated lifelength of about 0.2 m.

The CWT and lifetime map taken from the aft section are shown in Fig. 24. The lifetime map follows the behavior inferred from Fig. 20, i.e., there are fewer events detected and a greater percentage are long lifetime than either the center or forward sections. The aft section appears to be less able to support broadband behavior with most lifetime lines interrupted by voids. Below 600 Hz, the voided areas appear to be about the same size as those in the forward section. At 800 Hz and above, the lifetime map of the aft section data becomes sparse, with large voided areas. The differences in high-frequency behavior, as indicated in the lifetime maps of these three cases, may have resulted from the apparent differences in energy at the higher frequencies, as seen in the respective CWTs. The center section appears to have more high amplitude activity above 600 Hz than either the forward or aft section.

VII. Conclusions

Interval correlation analysis has been introduced using both a center referenced and first principal component referenced approach. The analyses calculate a property of coherent structure in the turbulent boundary layer related to correlation length. Termed lifelength, this property is based on an assumption of Gaussian distribution of the interval correlation over the sensor array. The Gaussian distribution was shown to be a conservative measure of long-life events when compared with the exponential distribution and predictions based on Efimtsov's correlation space scale. The analysis was extended and verified in the time/frequency domain using continuous wavelet transforms. The computation produces lifelength distributions at each analysis frequency and allows the retrieval of the time data that produced a specific result, thus yielding insight into the physical process that averaged statistics cannot provide. It was found that the use of the first principal component as reference often resulted in overestimation of the lifelength, especially in the case where too few sensors were available.

The analysis was extended to include lifetime maps where event lifetimes, as computed from the lifelengths, are plotted in the time/frequency domain. These plots showed evidence of large nonlinear structures, $\sim$2 m in length, as indicated by regions delineated by long-lifetime events. This suggested that long-lifetime events may not necessarily be coherent but may be better described as persistent. Based on these results, it is concluded that the interval correlation technique, and the associated lifelength distribution and lifetime map products, have been shown to yield accurate representations of the sidewall pressure characteristics of coherent structure in the turbulent boundary layer.

References

[1] Robinson, S. K., "Coherent Motions in the Turbulent Boundary Layer," *Annual Review of Fluid Mechanics*, Vol. 23, Jan. 1991, pp. 601–639. doi:10.1146/annurev.fl.23.010191.003125

[2] Gad-el-Hak, M., *Flow Control*, 1st ed., Cambridge Univ. Press, New York, 2000, Chaps. 2–5.

[3] Palumbo, D. L., and Chabalko, C., "Persistent Structures in the Turbulent Boundary Layer," *AIAA/CEAS Aeroacoustics Conference*, AIAA Paper 2854, 2005.

[4] Gupta, A. K., Laufer, J., and Kaplan, R. E., "Spatial Structure in the Viscous Sublayer," *Journal of Fluid Mechanics*, Vol. 50, No. 3, Dec. 1971, pp. 493–512. doi:10.1017/S0022112071002726

[5] Wallace, J. M., Eckelmann, H., and Brodkey, R. S., "Wall Region in Turbulent Shearflow," *Journal of Fluid Mechanics*, Vol. 54, No. 1, July 1972, pp. 39–48. doi:10.1017/S0022112072000515

[6] Corcos, G. M., "Resolution of Turbulent Pressures at the Wall of a Boundary Layer," *Journal of Sound and Vibration*, Vol. 6, No. 1, July 1967, pp. 59–70. doi:10.1016/0022-460X(67)90158-7

[7] Efimtsov, M. M., "Characteristics of the Field of Turbulent Wall Pressure Fluctuations at Large Reynolds Numbers," *Soviet Physics Acoustics*, Vol. 28, No. 4, July–Aug. 1982, pp. 491–497.

[8] Daubechies, I., *Ten Lectures On Wavelets*, Society for Industrial and Applied Mathematics, Philadelphia, PA, 1992.

[9] Holmes, P., Lumley, J. L., and Berkooz, G., *Turbulence, Coherent Structures, Dynamical Systems and Symmetry*, Cambridge Univ. Press, New York, 1996, pp. 86–113.

[10] Rizzi, S. A., Rackl, R. G., and Andrianov, E. V., "Flight Test Measurement from the TU-144ll Structure/Cabin Noise Experiment," NASA TM-2000-209858, 2000.

[11] Fox, R. W., and McDonald, A. T., *Introduction to Fluid Mechanics*, 4th ed., Wiley, New York, 1992, pp. 431–433.

[12] Rackl, R., and Weston, A., "Modeling of Turbulent Boundary Layer Surface Pressure Fluctuation Auto and Cross Spectra: Verifications and Adjustments Based on Tu-144ll Data," NASA TM-2005-213938, 2005.

[13] Anderson, E., Bai, Z., Bischof, C., Blackford, S., Demmel, J., Dongarra, J., Du Croz, J., Greenbaum, A., Hammarling, S., McKenney, A., and Sorensen, D., *LAPACK User's Guide*, 3rd ed., Society for Industrial and Applied Mathematics, Philadelphia, PA, 1999.

[14] Farge, M., "Wavelet Transforms and Their Applications to Turbulence," *Annual Review of Fluid Mechanics*, Vol. 24, Jan. 1992, pp. 395–457. doi:10.1146/annurev.fl.24.010192.002143

N. Clemens
Associate Editor